

Structure and magnetism of $\text{Cr}_2[\text{BP}_3\text{O}_{12}]$: Towards the “quantum–classical” crossover in a spin-3/2 alternating chain

O. Janson,^{1,*} S. Chen,¹ A. A. Tsirlin,^{1,2,†} S. Hoffmann,¹ J. Sichelschmidt,¹
Q. Huang,³ Z.-J. Zhang,⁴ M.-B. Tang,⁴ J.-T. Zhao,⁴ R. Kniep,¹ and H. Rosner^{1,‡}

¹Max Planck Institute for Chemical Physics of Solids, 01187 Dresden, Germany

²National Institute of Chemical Physics and Biophysics, 12618 Tallinn, Estonia

³NIST Center for Neutron Research, Gaithersburg, MD 20899, USA

⁴Key Laboratory of Transparent Opto-Functional Inorganic Materials
of Chinese Academy of Sciences, Shanghai 200050, PR China

(Dated: March 27, 2021)

Magnetic properties of the spin-3/2 Heisenberg system $\text{Cr}_2[\text{BP}_3\text{O}_{12}]$ are investigated by magnetic susceptibility $\chi(T)$ measurements, electron spin resonance, neutron diffraction, and density functional theory (DFT) calculations, as well as classical and quantum Monte Carlo (MC) simulations. The broad maximum of $\chi(T)$ at 85 K and the antiferromagnetic Weiss temperature of 139 K indicate low-dimensional magnetic behavior. Below $T_N = 28$ K, $\text{Cr}_2[\text{BP}_3\text{O}_{12}]$ is antiferromagnetically ordered with the $\mathbf{k} = 0$ propagation vector and an ordered moment of $2.5 \mu_B/\text{Cr}$. DFT calculations, including DFT+ U and hybrid functionals, yield a microscopic model of spin chains with alternating nearest-neighbor couplings J_1 and J'_1 . The chains are coupled by two nonequivalent interchain exchanges of similar strength (~ 1 – 2 K), but different sign (antiferromagnetic and ferromagnetic). The resulting spin lattice is quasi-one-dimensional and not frustrated. Quantum MC simulations show excellent agreement with the experimental data for the parameters $J_1 \simeq 50$ K and $J'_1/J_1 \simeq 0.5$. Therefore, $\text{Cr}_2[\text{BP}_3\text{O}_{12}]$ is close to the gapless critical point ($J'_1/J_1 = 0.41$) of the spin-3/2 bond-alternating Heisenberg chain. The applicability limits of the classical approximation are addressed by quantum and classical MC simulations. Implications for a wide range of low-dimensional $S = 3/2$ materials are discussed.

PACS numbers: 75.50.Ee, 75.30.Et, 75.10.Hk, 75.10.Jm, 75.10.Pq, 61.66.Fn

I. INTRODUCTION

Magnetic properties of transition-metal compounds are generally described with the Heisenberg spin Hamiltonian that may be augmented by additional terms responsible for the anisotropy. For example, the following Hamiltonian

$$H = \sum_{\langle ij \rangle} J \mathbf{S}_i \cdot \mathbf{S}_j - \sum_i D_i (\mathbf{S}_i \cdot \hat{z})^2 \quad (1)$$

accounts for a variety of experimental situations. Here, the first term describes the isotropic coupling J between spins on sites i and j , the second term is the single-ion anisotropy D_i , and \hat{z} is a unitary vector along z , whereas \mathbf{S}_i and \mathbf{S}_j are quantum-mechanical spin operators. Although a handful of solvable Heisenberg models exist,^{1,2} the complex algebra of the spin operators generally impedes analytical solutions.

A widely used approximation of a Heisenberg model is its classical treatment: the original quantum mechanical spin operators \mathbf{S}_i are replaced by real-space vectors \vec{S}_i . This transformation leads to enormous alleviation of the computational effort, even if the topology of exchange couplings is very intricate.

A fundamental limitation of classical models is their inability to account for quantum-mechanical singlets and the ensuing underestimation of the ground state (GS) energy. Indeed, for an antiferromagnetic (AF) exchange coupling J , the energy of the quantum-mechanical sin-

glet state $-JS(S+1)$ is always lower than the classical energy $-JS^2$ of the antiparallel spin arrangement. At the same time, the relative energy gain of a singlet scales as S^{-1} , thus being maximal for $S = 1/2$ and infinitesimal in the $S \rightarrow \infty$ limit.

Presently, there is an empirical evidence that for $S \geq 2$, classical models capture the essential physics and correctly reproduce the experimental magnetic behavior.^{3–5} In contrast, classical models often fail to predict the correct GS and magnetic excitation spectrum for the extreme “quantum” case of $S = 1/2$.^{6,7} Further on, many $S = 1$ systems, e.g., one-dimensional (1D) Haldane chains,⁸ can not be treated classically. Therefore, it is crucial to establish the applicability limits for the classical approximation, in order to distinguish between the “classical” cases amenable to a simplified model treatment, and the “quantum” cases that require the complete quantum-mechanical solution of the spin Hamiltonian.

A feasible way towards better understanding of these limits are real material studies, that allow for a direct comparison between theory and experiment. Previous work on the quantum-classical crossover rendered the quasi-1D $S = 3/2$ magnets as the relevant playground. Despite the relatively large spin of $3/2$, the pronounced one-dimensionality may lead to sizable quantum fluctuations and, thus, to deviations from the classical behavior. For example, inelastic neutron scattering (INS) studies of $\text{Cs}[\text{VX}_3]$ ($X = \text{Cl}, \text{Br}$) evidence that at high temperatures these materials are classical, while lowering

the temperature results in a crossover to the quantum behavior.⁹ The INS experiments on the quasi-1D magnet $\text{AgCr}[\text{P}_2\text{S}_6]$ yielded a sizable discrepancy between the observed spin-wave velocity and its classical value, thus indicating strong quantum effects that are present in $S=3/2$ chains.¹⁰

Here, we present a joint experimental and theoretical study of the quasi-1D $S=3/2$ system $\text{Cr}_2[\text{BP}_3\text{O}_{12}]$. Its crystal structure features magnetic $\text{Cr}(\text{III})_2\text{O}_9$ blocks embedded into a complex borophosphate framework (Fig. 1). Although this type of crystal structure could lead to the simple magnetism of isolated spin dimers, neutron diffraction and magnetic susceptibility measurements evidence long-range AF ordering at $T_N = 28\text{ K}$ that is indicative of sizable interdimer couplings. Using extensive density-functional theory (DFT) calculations, we evaluate a microscopic magnetic model for this compound and establish the spin lattice of weakly coupled bond-alternating Heisenberg chains. This theoretical model is in good agreement with the neutron scattering and magnetic susceptibility data.

As the microscopic magnetic model of $\text{Cr}_2[\text{BP}_3\text{O}_{12}]$ lacks frustration, its properties can be simulated with the computationally efficient quantum Monte Carlo (QMC) techniques. At the same time, the classical model on the same spin lattice can be treated using classical Monte Carlo (MC) algorithms. By comparing the QMC and classical MC results, we evaluate the relative impact of quantum as well as thermal fluctuations on the spin correlations, and in this way address the crossover between the quantum and classical behavior.

This paper is organized as follows. The experimental as well as numerical methods are described in Sec. II. The experimental part in Sec. III comprises the results of neutron diffraction, electron spin resonance (ESR), and magnetic susceptibility measurements. The DFT-based evaluation of the microscopic magnetic model (Sec. IV) is followed by the refinement of model parameters by means of QMC simulations and subsequent fitting to the experiment (Sec. V). The differences between the quantum model and its classical counterpart are discussed in Sec. VI. We summarize our results and give a short outlook in Sec. VII.

II. METHODS

$\text{Cr}_2[\text{BP}_3\text{O}_{12}]$ was prepared by the Pechini-type method.¹¹ 2.172 g chromium acetate (Alfa Aesar, 23.37(5) wt% chromium content) and 5.7945 g citric acid (Alfa Aesar 99+%) were dissolved in 50 ml water. 5 ml of glycerol (Sigma 99%) and a well-ground mixture of 0.3197 g boric acid (Sigma) and 1.7613 g ammonium dihydrogen phosphate (Merck) were added to the dark-green solution. After slow evaporation of water, a transparent resin was formed which was dried at 200 °C for 2 h. The obtained product was crushed and transferred to a corundum crucible. The first heating at 850 °C for 12 h yielded

a grey-green product. Several annealing steps with grinding in between followed. The final product was obtained after heat treatment at 1000 °C for 48 h.

The powder X-ray diffraction pattern (Huber image plate Guinier camera G670, Ge monochromator, $\text{Cu } K_{\alpha 1}$ radiation, $\lambda = 1.5406 \text{ \AA}$, powdered sample fixed with Vaseline between two Mylar foils each 6 μm thick) indicated the formation of single-phase $\text{Cr}_2[\text{BP}_3\text{O}_{12}]$.¹²

Neutron powder diffraction data were collected¹³ using the BT-1 high-resolution powder diffractometer at the NIST Center for Neutron Research. A monochromatic neutron beam with the wavelength of 1.5403 Å was produced by a $\text{Cu } (311)$ monochromator. Collimators with horizontal divergences of 15', 20', and 7' full width at half-maximum were used before and after the monochromator, and after the sample, respectively. The intensities were measured in steps of 0.05° in the 2θ range 3–168°. The data were collected at 4 K, 35 K, and 300 K. Additionally, the magnetic scattering was studied with the triple-axis spectrometer BT-7 using the wavelength of 2.359 Å . The intensity of the strongest magnetic reflection was monitored with the step of 0.5 K in the 5 – 35 K temperature range. The structural analysis was performed using the program **GSAS**.¹⁴ The magnetic structure was refined with **Fullprof**.¹⁵

The magnetic susceptibility was measured using a commercial Quantum Design MPMS SQUID in the temperature range 2–380 K in magnetic fields up to 5 T. The electron spin resonance (ESR) measurement was performed at room temperature with a standard continuous-wave spectrometer at X-band frequencies ($\nu \approx 9.5 \text{ GHz}$) by using a cylindrical resonator in TE_{012} mode.

DFT calculations have been performed using the full-potential local-orbital code FPLO9.00-33 (Ref. 16) and the pseudopotential projector-augmented-wave code VASP-5.2 (Ref. 17). For the scalar-relativistic calculations, we used the local density approximation (LDA)¹⁸ and generalized gradient approximation (GGA)¹⁹ exchange-correlation potentials. Spin-unpolarized calculations were performed on a $14 \times 14 \times 14$ mesh of k -points. For the spin-polarized calculations (DFT, DFT+ U), we doubled the cell along c and used a $4 \times 4 \times 2$ k -mesh. Hybrid-functional calculations were performed in VASP using the HSE06 functional²⁰ on a $2 \times 2 \times 2$ k -mesh.²¹ The convergence with respect to the k -meshes has been accurately checked. All calculations have been performed based on the crystal structure determined at 4 K, as given in Table I.

QMC simulations were performed using the code LOOPER from the software package ALPS version 1.3.²² The magnetic susceptibility was simulated on $8 \times 8 \times 64$ finite lattices of $S=3/2$ spins in the temperature range 0.25–8 J_1 , corresponding to 12.5–400 K (see Sec. V) using 30 000 sweeps for thermalization and 300 000 sweeps after thermalization. The statistical errors (<0.5%) are below the experimental accuracy. For simulations of the spin stiffness and the static structure factor, we used finite lattices up to 13 824 and 2 048 spins, respectively.

For the classical MC simulations, we used the SPINMC code,²² with 200 000 and 2 000 000 sweeps for and after thermalization, respectively. The length of the classical vectors is chosen such that the maximal diagonal correlation matches the exact quantum result. Chains of $N = 800$ spins were evaluated. Exact diagonalization of the $S^z = 0$ sector was performed for $N = 14$ sites alternating $S = 3/2$ chain using SPARSEDIAG from the ALPS package.²²

III. EXPERIMENTAL RESULTS

A. Crystal structure

The crystal structure of $\text{Cr}_2[\text{BP}_3\text{O}_{12}]$ has been initially refined from x-ray powder data in the space group $P3$.¹² However, the crystal structures of related $M(\text{III})_2[\text{BP}_3\text{O}_{12}]$ borophosphates were determined ($M = \text{In}$) or re-determined ($M = \text{Fe}$) from single crystal data in the space group $P6_3/m$.²³ This apparent mismatch led us to reconsider the crystal structure of $\text{Cr}_2[\text{BP}_3\text{O}_{12}]$. A thorough analysis of both X-ray and neutron powder patterns identified the reflection condition $00l$ with $l = 2n$, which is characteristic of the 6_3 screw axis. No other reflection conditions could be observed, so that the list of possible space groups is restricted to $P6_3$, $P6_3/m$, and $P6_322$. While the refinement in $P6_322$ was unsuccessful, the space group $P6_3/m$ resulted in low residuals and a fully ordered crystal structure. Therefore, this centrosymmetric space group was preferred over its non-centrosymmetric subgroup $P6_3$. No significant structural changes between 4 K and room temperature were detected. Crystallographic data are listed in Table I. Selected interatomic distances at 4 K are given in Table II.

The structure solution of $\text{Cr}_2[\text{BP}_3\text{O}_{12}]$ in the space group $P6_3/m$ is consistent with earlier results for other $M_2[\text{BP}_3\text{O}_{12}]$ transition-metal borophosphates.²³ Their crystal structures are isotypic and feature dimers of face-sharing MO_6 octahedra (Fig. 1, bottom). The octahedra exhibit a sizable trigonal distortion leading to two groups of nonequivalent Cr–O distances. The shorter Cr–O3 distances of about 1.91 Å (at 4 K) take the terminal position of the Cr_2O_9 dimer, whereas the longer Cr–O1 distances of about 2.04 Å are bridging (Fig. 1, bottom right). The formation of longer Cr–O distances in the bridging position is due to the Cr–Cr contact remaining relatively long (about 2.8 Å), in order to reduce the repulsion between the positively charged Cr^{3+} ions. PO_4 tetrahedra link the Cr_2O_9 dimers along $[0001]$, whereas the BO_3 triangles interconnect the PO_4 tetrahedra and do not share oxygen atoms with the CrO_6 octahedra (Fig. 1, top).

B. Magnetic structure

At 4 K, an additional magnetic scattering was observed. The only visible magnetic reflection is at $2\theta \simeq$

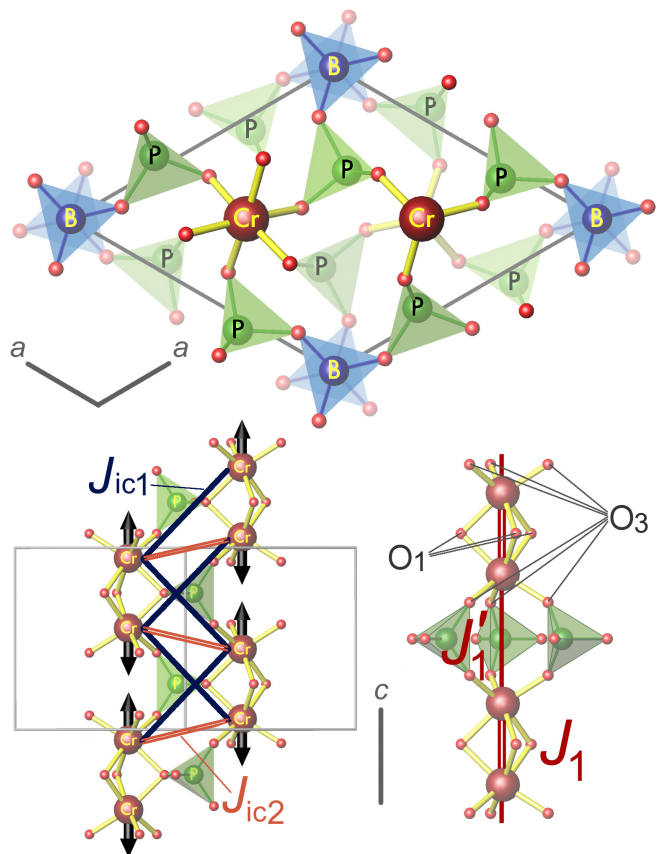


FIG. 1. (Color online) Crystal structure of $\text{Cr}_2[\text{BP}_3\text{O}_{12}]$. Top: view along $[0001]$. Bottom left panel: view perpendicular to $[0001]$. The pathways of the leading interchain couplings J_{ic1} and J_{ic2} are shown with dark gray (dark blue) and light gray (red) lines, respectively. Thick arrows denote the experimental magnetic structure refined in Γ_1 (see Sec. III B for details). Bottom right panel: dimers are connected via three PO_4 tetrahedra and form chains running along $[0001]$. The intra-dimer coupling J_1 (double line) as well as the interdimer coupling J'_1 (single line) are shown.

17.6° and matches the weak 101 reflection of the nuclear structure. As the Néel temperature of $\text{Cr}_2[\text{BP}_3\text{O}_{12}]$ is $T_N \simeq 28$ K (see below) and no structural changes below T_N are expected, the subtraction of the 35 K data from the 4 K data results in the purely magnetic scattering (Fig. 2, inset). However, no clear signatures of other magnetic reflections could be observed.

According to Basireps, the $P6_3/m$ space group, the $\mathbf{k} = 0$ propagation vector, and the $4f$ Wyckoff position of Cr allow for 12 irreducible representations with the magnetic moments lying in the ab plane or pointing along the c direction. Most of these representations can be discarded because they produce the largest magnetic reflection at 100, 110, or 111, which is contrary to the experimental observation of the magnetic scattering at 101 (Fig. 2, inset). The refinement is possible only in two representations, Γ_1 and Γ_9 , that entail same ordering

TABLE I. Crystallographic data for $\text{Cr}_2[\text{BP}_3\text{O}_{12}]$ (space group $P6_3/m$) according to the neutron powder diffraction data at 4, 35 and 300 K.

| T | | 4 K | | | 35 K | | | 300 K | | |
|-----------------------|-----|-----------|-----------|-----------|-----------|-----------|-----------|-----------|-----------|-----------|
| a (Å) | | 7.9444(2) | | | 7.9448(2) | | | 7.9524(2) | | |
| c (Å) | | 7.3439(3) | | | 7.3448(3) | | | 7.3543(3) | | |
| V (Å ³) | | 401.40(2) | | | 401.49(3) | | | 402.78(3) | | |
| R_p (%) | | 5.5 | | | 5.8 | | | 6.4 | | |
| R_{wp} (%) | | 6.9 | | | 7.6 | | | 7.9 | | |
| R_{exp} (%) | | 6.1 | | | 7.5 | | | 8.4 | | |
| | | x/a | y/b | z/c | x/a | y/b | z/c | x/a | y/b | z/c |
| Cr | 4f | 1/3 | 2/3 | 0.0578(8) | 1/3 | 2/3 | 0.0614(9) | 1/3 | 2/3 | 0.0590(7) |
| P | 6h | 0.3657(4) | 0.3166(5) | 1/4 | 0.3658(4) | 0.3168(5) | 1/4 | 0.3653(4) | 0.3159(5) | 1/4 |
| B | 2a | 0 | 0 | 1/4 | 0 | 0 | 1/4 | 0 | 0 | 1/4 |
| O1 | 6h | 0.4023(4) | 0.5254(4) | 1/4 | 0.4009(4) | 0.5249(5) | 1/4 | 0.3997(4) | 0.5255(5) | 1/4 |
| O2 | 6h | 0.1362(4) | 0.1931(4) | 1/4 | 0.1351(5) | 0.1924(4) | 1/4 | 0.1358(4) | 0.1926(4) | 1/4 |
| O3 | 12i | 0.4368(3) | 0.2691(3) | 0.0774(2) | 0.4365(3) | 0.2697(4) | 0.0768(3) | 0.4382(3) | 0.2716(3) | 0.0786(3) |

TABLE II. Selected interatomic distances (in Å) in the $\text{Cr}_2[\text{BP}_3\text{O}_{12}]$ crystal structure at 4 K.

| | | | |
|-------|---------------------|------|---------------------|
| Cr–O1 | $3 \times 2.041(5)$ | P–O1 | 1.535(4) |
| Cr–O3 | $3 \times 1.910(3)$ | P–O2 | 1.580(4) |
| Cr–Cr | 2.823(11) | P–O3 | $2 \times 1.511(2)$ |
| B–O2 | $3 \times 1.365(3)$ | | |

pattern (Fig. 1, bottom left) with the magnetic moments along c and a , respectively.

To evaluate the ordered magnetic moment, we refined the subtracted pattern as the purely magnetic phase, and fixed the scale factor according to the refinement of the 35 K pattern, which is free from magnetic scattering. The resulting magnetic moment at 4 K is $2.5(1) \mu_B$ in Γ_1 and $1.1(1) \mu_B$ in Γ_9 , with the refinement residuals of 0.131 in both models. While the refinements within Γ_1 and Γ_9 are slightly different at high angles (see the inset of Fig. 2), the quality of the powder data is insufficient to observe these marginal differences and to discriminate between the two models. However, the spin-only magnetic moment of $3 \mu_B$, which is expected for the $S = 3/2$ Cr^{3+} ion, strongly favors the solution in Γ_1 . The somewhat lower experimental value of $2.5 \mu_B$ is due to quantum fluctuations (see Sec. V).

The magnetic structure of $\text{Cr}_2[\text{BP}_3\text{O}_{12}]$ is shown in Fig. 1 (bottom left). We find that the Cr moments are antiferromagnetically ordered within each Cr_2O_9 dimer. The interdimer ordering is also AF, both in the ab plane and along the c direction.

Temperature evolution of the magnetic moment can be tracked by the temperature dependence of the magnetic reflection 101 (Fig. 2). These data are fitted with the empirical formula

$$I(T) = I_{bg} + I_0 \left(1 - \frac{T}{T_N}\right)^\beta, \quad (2)$$

where I_{bg} refers to the nuclear scattering and back-

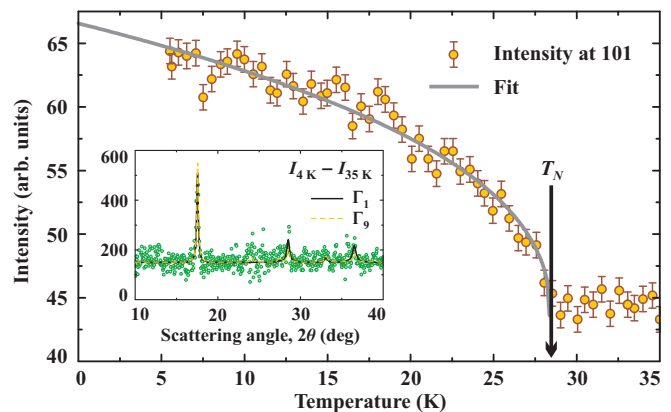


FIG. 2. (Color online) $\text{Cr}_2[\text{BP}_3\text{O}_{12}]$: temperature evolution of the magnetic 101 reflection (circles) and the fit with Eq. (2). The residual intensity above T_N is due to the nuclear scattering and background. Inset: refinement of the subtracted ($I_{4K} - I_{35K}$) pattern with spins along c (Γ_1 , dark solid line) and along a (Γ_9 , light dashed line). Note that the temperature scan (main figure) and the angular scan (inset) are done on different instruments, hence the respective intensities should not be compared.

ground above T_N . The fit yields the Néel temperature $T_N = 28.2(7)$ K and the critical exponent $\beta = 0.38(3)$. The estimated $T_N \simeq 28$ K is in excellent agreement with the magnetic susceptibility measurement presented below (Fig. 3), whereas β falls into the range of values (0.36–0.39) proposed for the 3D Heisenberg model.²⁴

C. Magnetic susceptibility and ESR

The temperature dependence of the magnetic susceptibility $\chi(T)$ (Fig. 3, top) reveals a typical low-dimensional behavior with a broad maximum around $T = 85$ K. The high-temperature part ($T > 200$ K) of the curve obeys the Curie-Weiss law (Fig. 3, bottom left) with the Curie con-

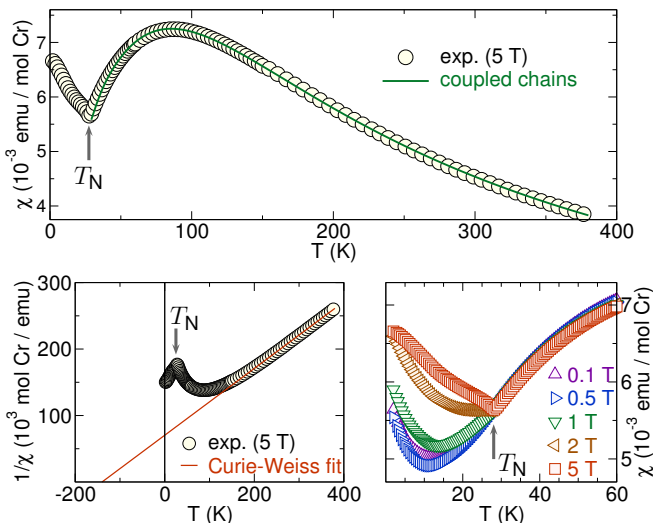


FIG. 3. (Color online) Top panel: Experimental magnetic susceptibility $\chi(T)$ of $\text{Cr}_2[\text{BP}_3\text{O}_{12}]$ measured at 5 T (circles) and fit with the model of coupled bond-alternating $S=3/2$ chains (line). Bottom left panel: Curie-Weiss fit to experimental $\chi(T)$. Bottom right panel: Field dependence of $\chi(T)$. Note the long-range AF ordering transition at $T_N = 28$ K.

stant $C = 1.987 \text{ emu K (mol Cr)}^{-1}$ leading to the effective magnetic moment $\mu_{\text{eff}} = \sqrt{3 C k_B \mu_B^{-2} N_A^{-1}} = 3.987 \mu_B$ per Cr, which is slightly larger than the spin-only contribution $\mu_{\text{eff}} = g\sqrt{S(S+1)} \simeq 3.88 \mu_B$ (assuming the orbital moment is completely quenched).

The Weiss temperature $\theta = 139$ K and the broad maximum around $T^{\text{max}} = 85$ K, corresponding to $\sim 61\%$ of θ , indicate sizable AF spin correlations. The magnetic ordering temperature $T_N = 28$ K can be clearly traced by the divergence of the $\chi(T)$ curves measured in low and high fields. While the low-field measurements show only an inconspicuous bend around T_N , the measurements above 2 T reveal a well-defined cusp. This divergence is due to the spin-flop transition in the AF-ordered phase. The spin-flop transition indeed takes place at about 1.7 T, as shown by the low-temperature magnetization curve.²⁵

Room-temperature ESR measurements yield a narrow line that can be fitted with a single powder-averaged Lorentzian.²⁵ Within resolution, the resonance field appears isotropic and corresponds to the g value of 1.968 which indicates weak spin-orbit coupling, as typical for Cr^{3+} .

The low-dimensional magnetism of $\text{Cr}_2[\text{BP}_3\text{O}_{12}]$ is consistent with the presence of Cr_2O_9 dimers in the crystal structure. However, isolated spin dimers should have a singlet GS at low temperatures. The fact that $\text{Cr}_2[\text{BP}_3\text{O}_{12}]$ develops long-range AF order with a sizable Néel temperature of 28 K implies substantial interdimer couplings via the PO_4 groups. While such couplings are abundant in vanadium and copper phosphates,^{26–28} their identification is by no means a simple task. For exam-

ple, in $\text{Cr}_2[\text{BP}_3\text{O}_{12}]$ the shortest interdimer Cr–Cr distances are 4.55 Å along [0001] and 4.67 Å in the (0001) plane, and it is impossible to decide *a priori* whether one of these pathways is more efficient, or both should be treated on equal footing. To develop a reliable magnetic model of $\text{Cr}_2[\text{BP}_3\text{O}_{12}]$, we perform extensive DFT calculations followed by QMC simulations, and provide detailed microscopic insight into the magnetism of this compound.

IV. DFT CALCULATIONS

To unravel the microscopic origin of the observed low-dimensional magnetic behavior, we apply DFT calculations and evaluate the individual exchange couplings. Nonmagnetic (spin-unpolarized) calculations within both LDA and GGA yield a well-structured valence band (Fig. 4, top) with the total width of ~ 10 eV, crossed by the Fermi level ε_F at zero energy. This metallic electronic GS, contrasting with the green color of $\text{Cr}_2[\text{BP}_3\text{O}_{12}]$, originates from the underestimation of the strong electron-electron repulsion within the Cr $3d$ shell. Technically, the band gap can be readily restored in a spin-polarized calculation, due to the sizable exchange splitting typical for Cr^{3+} . However, its value is too small (1.29 eV in LSDA, 1.78 eV in GGA)²⁵ to account for the green color ($\simeq 2.2$ – 2.5 eV) of $\text{Cr}_2[\text{BP}_3\text{O}_{12}]$. Accounting for electronic correlations is challenging, since many-body effects can not be properly described within the one-electron approach of conventional DFT functionals.

Typically, multiorbital correlated insulators are described by an extended Hubbard model that comprises the kinetic terms (electron transfer), the on-site and intersite correlations (Coulomb repulsion), and the on-site exchange (Hund’s exchange). However, the large Hilbert space of such models impedes even an approximate numerical solution that would establish a simple relation between the parameters of the Hubbard model and the resulting magnetic couplings. Therefore, we restrict ourselves to a qualitative analysis of electron transfers.

For the quantitative evaluation of magnetic couplings, we account for correlation effects using the mean-field-like DFT+ U approach or the hybrid (DFT + exact exchange) functionals. The comparison to the experiment demonstrates the good agreement between different computational approaches, and underscores the validity of the qualitative analysis based on the electron transfers. Thus, this qualitative model approach could also be used as a starting point for more involved Cr^{3+} systems with nontrivial coupling pathways.

A. Qualitative model approach

Conventional DFT (LDA and GGA) functionals are known for their accurate description of electron transfer

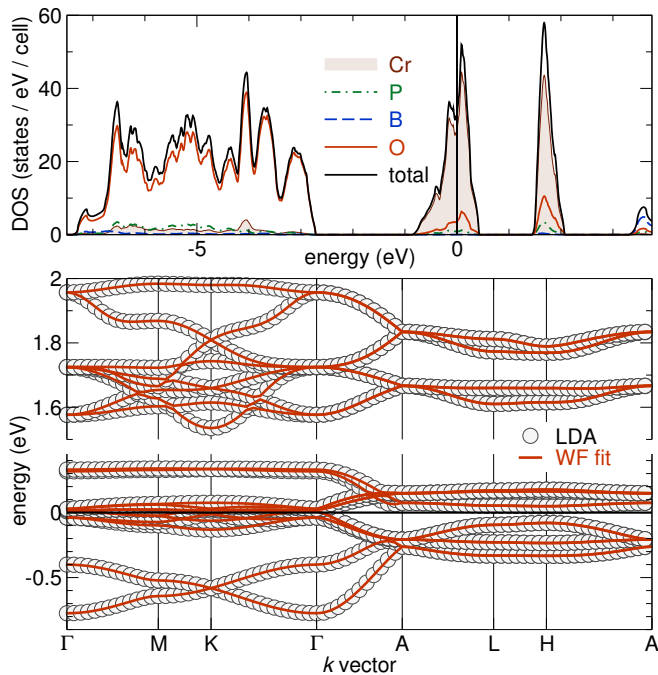


FIG. 4. (Color online) Electronic structure of $\text{Cr}_2[\text{BP}_3\text{O}_{12}]$. Top: LDA density of states. The Fermi level ε_F is at zero energy. The contribution from Cr states is shown by shaded filling. Bottom: LDA bands in the vicinity of the Fermi level and the fit with the tight-binding model based on Wannier functions.

processes, thus kinetic terms of the model Hamiltonian can be evaluated directly from the LDA/GGA band dispersions for the Cr 3d states. Typical for an octahedral environment, these states split into two manifolds: half-filled t_{2g} orbitals centered at ε_F , and empty e_g orbitals that lie $\sim 1.7\text{eV}$ higher in energy owing to the sizable crystal-field splitting.

Altogether, the t_{2g} and e_g manifolds comprise 20 bands, in line with five 3d orbitals per Cr atom and four Cr atoms in a unit cell. To evaluate the transfer integrals $t_{ij}^{mm'}$ (m and m' are orbital indices, i and j are site indices), we map these 20 bands onto an effective five-orbital tight-binding model, and parameterize this model using the Wannier functions (WF) technique.²⁹ In the WF basis (Fig. 5), the couplings $t_{ij}^{mm'}$ are evaluated as nondiagonal matrix elements. The resulting $t_{ij}^{mm'}$ show excellent agreement between the tight-binding model and the computed LDA/GGA band dispersions (Fig. 4, bottom).

Sizable transfer integrals are found for four Cr–Cr pathways (Table III): the intradimer transfer (t_1), the interdimer transfer along c (t'_1), the shortest interdimer pathway in the ab plane (t_{ic2}), and the longer interdimer pathway along the $[2\bar{2}3]$ direction (t_{ic1}), see Fig. 1. Here, t'_1 and t_{ic2} run via triple bridges of the PO_4 polyhedra (along c), whereas t_{ic1} runs via a single PO_4 tetrahedron. Other couplings are negligible, as they involve the transfer through at least two PO_4 tetrahedra in a row.

TABLE III. Leading transfer integrals $t_i^{mm'}$ (notation according to Fig. 1), where m and m' are orbital indices from the following set: $|xy\rangle$, $|xz\rangle$, $|yz\rangle$, $|z^2 - r^2\rangle$, and $|x^2 - y^2\rangle$. All values are given in meV. For clarity, only one of two symmetrically equivalent terms $t_{ij}^{mm'}$ and $t_{ij}^{m'm}$ is shown. The Cr–Cr distances ($d_{\text{Cr-Cr}}$) are given for the 4 K structure (Table I).

| t_1 ($d_{\text{Cr-Cr}} = 2.823 \text{ \AA}$) | | | | | |
|---|--------------|--------------|--------------|---------------------|---------------------|
| | $ xy\rangle$ | $ xz\rangle$ | $ yz\rangle$ | $ z^2 - r^2\rangle$ | $ x^2 - y^2\rangle$ |
| $\langle xy $ | -38 | -125 | -125 | -97 | - |
| $\langle xz $ | - | -38 | -125 | 39 | -89 |
| $\langle yz $ | - | - | -38 | 58 | 78.9 |
| $\langle z^2 - r^2 $ | - | - | - | - | - |
| $\langle x^2 - y^2 $ | - | - | - | - | - |
| t'_1 ($d_{\text{Cr-Cr}} = 4.521 \text{ \AA}$) | | | | | |
| | $ xy\rangle$ | $ xz\rangle$ | $ yz\rangle$ | $ z^2 - r^2\rangle$ | $ x^2 - y^2\rangle$ |
| $\langle xy $ | -124 | - | - | - | - |
| $\langle xz $ | - | -124 | - | 33 | - |
| $\langle yz $ | - | - | -124 | - | - |
| $\langle z^2 - r^2 $ | - | - | - | -60 | - |
| $\langle x^2 - y^2 $ | - | - | - | - | -60 |
| t_{ic1} ($d_{\text{Cr-Cr}} = 5.875 \text{ \AA}$) | | | | | |
| | $ xy\rangle$ | $ xz\rangle$ | $ yz\rangle$ | $ z^2 - r^2\rangle$ | $ x^2 - y^2\rangle$ |
| $\langle xy $ | - | - | - | 86 | -60 |
| $\langle xz $ | - | - | - | -44 | 75 |
| $\langle yz $ | - | - | - | -67 | - |
| $\langle z^2 - r^2 $ | - | - | - | 30 | 35 |
| $\langle x^2 - y^2 $ | - | - | - | - | 38 |
| t_{ic2} ($d_{\text{Cr-Cr}} = 4.665 \text{ \AA}$) | | | | | |
| | $ xy\rangle$ | $ xz\rangle$ | $ yz\rangle$ | $ z^2 - r^2\rangle$ | $ x^2 - y^2\rangle$ |
| $\langle xy $ | - | -30 | -30 | - | - |
| $\langle xz $ | - | - | - | - | - |
| $\langle yz $ | - | - | - | - | - |
| $\langle z^2 - r^2 $ | - | - | - | - | - |
| $\langle x^2 - y^2 $ | - | - | - | - | -31 |

Although an explicit expression relating exchange integrals J_{ij} to transfer integrals $t_{ij}^{mm'}$ is presently not available, the qualitative comparison of $t_{ij}^{mm'}$ terms elucidates different contributions to the magnetic exchange. According to the Goodenough-Kanamori rules, the hoppings between the half-filled states (both m and m' belong to the t_{2g} subspace) are responsible for AF couplings, whereas the hoppings between the half-filled and empty states (m belongs to t_{2g} , m' belong to e_g) give rise to ferromagnetic (FM) interactions.

First, we consider the intradimer $t_1^{mm'}$ hoppings, where the couplings between different t_{2g} orbitals are dominant:

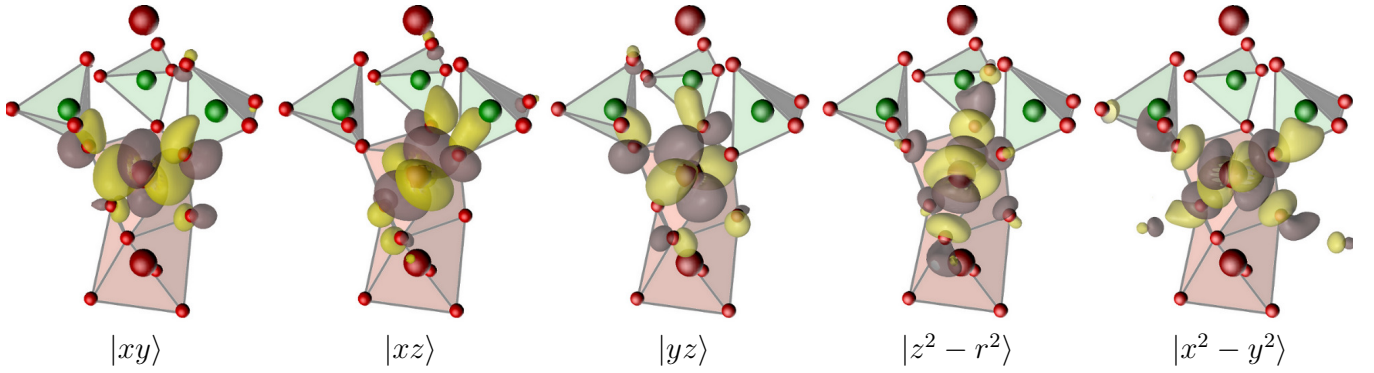


FIG. 5. (Color online) $\text{Cr}_2[\text{BP}_3\text{O}_{12}]$: Wannier functions for five Cr $3d$ orbitals (see subscripts). Cr, P and O atoms are depicted by large (red), intermediate-size (green) and small (red) spheres, respectively. For each of the five Wannier functions, a Cr_2O_9 dimer and three PO_4 tetrahedra are shown. The projection is similar to the bottom right panel of Fig. 1.

$t_1^{xy,xz} = t_1^{xz,yz} = t_1^{yz,xy} = -125$ meV. At the same time, the largest hopping between the t_{2g} and e_g orbitals is smaller ($t_1^{xy,z^2-r^2} = -97$ meV), thus hinting at the AF nature of J_1 . For the interdimer coupling t'_1 the difference is even more pronounced: the hoppings between t_{2g} orbitals amount to -124 meV, thus dominating over the hopping to the empty $z^2 - r^2$ orbital. Therefore, the interdimer exchange J'_1 should be also AF.

The interchain coupling J_{ic2} is realized primarily via $t_{ic2}^{xy,xz}$ and $t_{ic2}^{xy,yz}$ hoppings, hence the AF contribution is again dominant. In contrast, for the interchain coupling J_{ic1} , the $t_{2g} \rightarrow t_{2g}$ hoppings are close to zero, whereas the $t_{2g} \rightarrow e_g$ hoppings are still sizable. Therefore, the overall exchange should be FM.

The above qualitative analysis is confirmed by elaborate DFT+ U and hybrid-functional calculations reported below. More importantly, the proposed couplings are in agreement with the experimental magnetic structure that features antiparallel spins along J_1 , J'_1 , and J_{ic2} (Fig. 1, bottom left panel). The respective AFM couplings establish parallel spins along the J_{ic1} bonds that are indeed FM. Therefore, the spin lattice of $\text{Cr}_2[\text{BP}_3\text{O}_{12}]$ is non-frustrated. Because $J'_1 \gg J_{ic1}, J_{ic2}$, this spin lattice can be considered as quasi-1D, with bond-alternating $J_1 - J'_1$ chains running along the c direction.

B. Total-energy calculations

A sizable exchange splitting typical for Cr^{3+} compounds readily opens a band gap (albeit underestimating the experimental value, see Ref. 25) in the spin-polarized calculations, so that the magnetic energy can be evaluated directly from LSDA or GGA total-energy calculations. In particular, total energies E_{tot} corresponding to different collinear magnetic configurations can be mapped onto classical Heisenberg model, thus yielding the exchange integrals J_{ij} :

$$E_{\text{tot}} = E_0 + E_{\text{magn}} = E_0 + \sum_{\langle i,j \rangle} J_{ij} \vec{S}_i \cdot \vec{S}_j. \quad (3)$$

We apply this approach to evaluate the intrachain and interchain couplings. In LSDA, we obtain $J_1 = 151$ K and $J'_1 = 82$ K as well as the FM $J_{ic1} = -8$ K and the AF $J_{ic2} = 2$ K. Spin-polarized GGA yields marginally smaller values (Table IV). To challenge these estimates, we address the Weiss temperature θ , which is a linear combination of magnetic couplings.³⁰ For the $\text{Cr}_2[\text{BP}_3\text{O}_{12}]$ spin lattice, the expected Weiss temperature is:

$$\theta = \frac{1}{3} S(S+1)(J_1 + J'_1 + 6J_{ic1} + 3J_{ic2}), \quad (4)$$

where each coupling is summed up according to its coordination number in the spin lattice. Adopting the values of J_i from LSDA (GGA), we obtain $\theta \simeq 242$ K (202 K), which is 50–70% larger than the experimental value $\theta = 139$ K.

This discrepancy primarily originates from the poor description of electronic correlations within LDA or GGA, and calls for the application of more elaborate computational approaches. For strongly correlated insulators, such as $\text{Cr}_2[\text{BP}_3\text{O}_{12}]$, the mean-field DFT+ U method is a natural choice. An intrinsic problem of this method is the double counting (DC) of the correlation energy already present in LDA or GGA. This correlation energy should be subtracted from the total energy of the system. In the widely used DC corrections, denoted around-mean-field (AMF) and fully-localized limit (FLL),³¹ the subtracted energy corresponds to the energy of the uniformly occupied state or the state with integer occupation numbers, respectively. Previous DFT+ U studies on Cr^{3+} materials³² did not render any of the two schemes preferable, thus we apply both and compare their results with the experiment.

Besides the DC, the DFT+ U method introduces two free parameters: the on-site repulsion U_d and the on-site exchange J_d . While an empirical evidence favors $J_d \simeq$

1 eV for 3d elements, the values of U_d can substantially vary depending on the electronic configuration and local environment of the magnetic ion. For Cr^{3+} , we varied U_d in the range between 2 and 4 eV.^{32,33}

The resulting DFT+ U -based exchange integrals are listed in Table IV. We find that the exchange integrals are weakly dependent on the DFT exchange-correlation potential (LSDA or GGA). In contrast, the DC correction plays a more substantial role: the calculations within AMF yield considerably larger couplings than the calculations within FLL for the same value of U_d . Besides, J_{ic1} turns out to be AF in AMF, but FM in FLL. This conspicuous difference between different flavors of DFT+ U necessitates an additional examination of this problem by an independent technique.

To this end, we resort to the HSE06 hybrid functional that is free from the DC problem. Here, the DFT exchange is mixed with a fraction of exact (Hartree-Fock) exchange.³⁴ The HSE06-based exchange integrals (Table IV) are very similar to those obtained using DFT+ U FLL with $U_d=3.0$ eV. To check the stability of the HSE06 results, we varied the parameter β , which reflects the admixture of the exact exchange to the standard DFT exchange ($\beta=0.25$ in the original definition of HSE06). As follows from the resulting values (Table IV), the increase in β from 0.2 to 0.3 is accompanied by the $\sim 25\%$ reduction in the exchange couplings, while the J'_1/J_1 ratio is essentially unchanged. Therefore, the effects of increasing β in HSE06 and increasing U_d in DFT+ U are somewhat similar, despite the disparate physical meaning of the U_d and β parameters.

On a qualitative level, DFT+ U FLL, hybrid functionals, and model approach concur with each other on the nature of magnetic couplings in $\text{Cr}_2[\text{BP}_3\text{O}_{12}]$. By contrast, DFT+ U AMF predicts the different sign of J_{ic1} , which would render the spin lattice weakly frustrated. However, this scenario looks very unlikely because the independent model analysis (Sec. IV A) yields FM J_{ic1} . Additionally, DFT+ U AMF systematically overestimates the absolute values of J_1 and J'_1 (see experimental values in Sec. V) and should probably be discouraged in the case of $\text{Cr}_2[\text{BP}_3\text{O}_{12}]$.³⁵

Apart from the overall energy scale of J_1 and J'_1 that is dependent on U_d or β (Table IV), different flavors of DFT+ U as well as HSE06 predict different J'_1/J_1 ratios. Our computational results yield $J'_1/J_1 = 0.39 - 0.94$, so that J'_1 is smaller than J_1 but certainly large enough to ensure the quasi-1D nature of the spin lattice. Unfortunately, the more precise evaluation of the J'_1/J_1 ratio lies beyond the capabilities of present-day DFT-based techniques and should be addressed by numerical simulations of the spin model and subsequent fitting to the experimental data (see Sec. V).

Finally, we take into account the spin-orbit (SO) coupling, and quantify the single-ion anisotropy D using the DFT+ U +SO calculations within the FLL in VASP. To this end, we calculate total energies (Fig. 1, bottom left) of the AF GS with the magnetic moments aligned paral-

TABLE IV. Leading exchange integrals J_i (in K) calculated with different DFT-based methods. For the DFT+ U results, the double-counting correction (DCC) and U_d value (in eV) are given. For the HSE06 hybrid functional, the admixture of the exact exchange (β) is specified.

| E_{xc} (DCC) | U_d or β | J_1 | J'_1 | J_{ic2} | J_{ic1} | J'_1/J_1 |
|-----------------------|------------------|-------|--------|------------------|------------------|------------|
| LSDA | | 150 | 82 | 2.5 | -7.8 | 0.55 |
| GGA | | 125 | 63 | 2.2 | -5.6 | 0.51 |
| LSDA+ U (AMF) | 2.0 | 109 | 60 | 2.3 | 0.1 | 0.62 |
| | 3.0 | 89 | 55 | 2.2 | 1.7 | 0.72 |
| | 4.0 | 70 | 50 | 2.1 | 2.8 | 0.86 |
| LSDA+ U (FLL) | 2.0 | 84 | 49 | 1.6 | -2.1 | 0.58 |
| | 3.0 | 54 | 38 | 1.2 | -1.8 | 0.71 |
| | 4.0 | 33 | 31 | 0.9 | -1.6 | 0.94 |
| GGA+ U (AMF) | 2.0 | 97 | 48 | 2.2 | 1.0 | 0.50 |
| | 3.0 | 81 | 44 | 2.1 | 2.3 | 0.54 |
| | 4.0 | 67 | 41 | 2.1 | 3.3 | 0.61 |
| GGA+ U (FLL) | 2.0 | 78 | 40 | 1.6 | -1.0 | 0.51 |
| | 3.0 | 54 | 32 | 1.2 | -1.0 | 0.59 |
| | 4.0 | 37 | 26 | 1.0 | -0.9 | 0.69 |
| HSE06 | 0.20 | 66 | 27 | 1.2 | -2.5 | 0.41 |
| | 0.25 | 58 | 23 | 1.0 | -2.0 | 0.40 |
| | 0.30 | 51 | 20 | 0.9 | -1.7 | 0.39 |

lel and perpendicular to the hexagonal axis (c -axis). For $U_d = 3$ eV, the energy difference of 1.3 K slightly favors the in-plane spin arrangement. This result implies a very weak single-ion anisotropy. However, the direction of the magnetic moment should be determined experimentally because the energy difference of 1 K is on the verge of the accuracy of DFT.

In summary, our band structure calculations arrive at a scenario of Heisenberg spin chains with two alternating nearest-neighbor AF interactions J_1 and J'_1 . The magnetic chains are weakly coupled in a non-frustrated manner by the FM J_{ic1} and the AF J_{ic2} . While both interchain couplings are apparently weak (below 2 K in terms of the absolute value), the energy scale of the intrachain couplings, as well as the precise alternation ratio, are rather sensitive to details of the computational procedure and require further refinement applying simulation techniques to fit the experimental data.

V. QMC SIMULATIONS AND COMPARISON WITH THE EXPERIMENTS

To refine the parameters of the microscopic magnetic model, we simulate the temperature dependence of the reduced magnetic susceptibility χ^* for various ratios of J'_1/J_1 , while keeping the interchain couplings constant $J_{\text{ic2}} = -J_{\text{ic1}} = 0.02J_1$ (see Table IV), and subsequently fit the simulated QMC curves to the experiment using the expression:

TABLE V. Results of QMC simulations and fitting to the experimental magnetic susceptibility. J_1 and g are obtained from the fits to $\chi(T)$. T_N/J_1 is obtained from simulations of spin stiffness (see text). S_∞ is evaluated using Eq. (6). T_N and m are scaled using J_1 and g from columns 2 and 3.

| J'_1/J_1 | J_1 (K) | g | T_N/J_1 | T_N (K) | S_∞ | $m(\mu_B)$ |
|------------|-----------|-------|-----------|-----------|------------|------------|
| 0.4 | 51.84 | 2.006 | 0.584 | 30.27 | 1.128 | 2.22 |
| 0.5 | 49.51 | 2.002 | 0.642 | 31.79 | 1.151 | 2.27 |
| 0.6 | 47.10 | 1.996 | 0.689 | 32.45 | 1.164 | 2.29 |
| 0.7 | 44.78 | 1.993 | 0.726 | 32.51 | 1.169 | 2.30 |
| 0.8 | 42.58 | 1.992 | 0.755 | 32.15 | 1.165 | 2.29 |

$$\chi(T) = \frac{N_A g^2 \mu_B^2}{k_B J_1} \cdot \chi^* \left(\frac{T}{k_B J_1} \right) + \chi_0. \quad (5)$$

Here, the fitted parameters are J_1 , the Landé factor g , and the temperature-independent contribution χ_0 .³⁶ The results are presented in Table V (columns 2 and 3). A general trend is the decrease in J_1 upon the increase in J'_1/J_1 , so that the sum of the leading couplings $J_1 + J'_1$ remains nearly constant (74.5 ± 2.0 K), see also Eq. (4). Still, smaller values of J'_1/J_1 yield better agreement with the experimental curve, especially around the maximum in $\chi(T)$.

In general, additional restrictions for the model parameters can be set by the fitted values of g . However, g is marginally dependent on J'_1/J_1 and shows good agreement with the ESR value of 1.968 in the whole range studied. Therefore, simulation of further measurable quantities is needed to refine the model parameters.

First, we address the magnetic ordering temperature. To this end, we calculate the spin stiffness ρ as a function of temperature for finite lattices with up to $N = L_x \times L_y \times L_z = 13824$ spins. At the magnetic ordering transition temperature, the products $\rho_i L_i$ ($i = x, y, z$) are independent of L_i . Thus, T_N is the temperature at which the $\rho L(T)$ curves of the different finite lattices cross. The difference between the simulated values of T_N and its experimental value of 28 K is below 10% for the whole range of J'_1/J_1 (see columns 4 and 5 of Table V). Similar to the fits of $\chi(T)$, lower values of J'_1/J_1 yield slightly better agreement with the experimental $T_N = 28$ K.

Another measured quantity, which can be used for comparisons between theory and experiment, is the ordered magnetic moment m . In the classical $S = 3/2$ Heisenberg model, the ordered magnetic moment $m = g\mu_B S$ amounts to $3\mu_B$, but the experimentally observed moment in $\text{Cr}_2[\text{BP}_3\text{O}_{12}]$ is substantially smaller ($2.5\mu_B$, see Sec. III B). We estimate the reduction in m due to quantum fluctuations. To this end, we simulate the magnetic structure factors \mathbb{S} for finite lattices containing up to 2048 spins.

For the propagation vector \mathbf{k} of the magnetically ordered GS, the ordered magnetic moment m is evaluated

using the finite-size scaling procedure:

$$\frac{3\mathbb{S}(\mathbf{k})}{N} = S_\infty(\mathbf{k})^2 + \frac{\sigma_1}{\sqrt{N}} + \frac{\sigma_2}{N} \quad (6a)$$

$$m = g\mu_B S_\infty(\mathbf{k}), \quad (6b)$$

where the fitting parameters are $S_\infty(\mathbf{k})$ as well as the expansion coefficients σ_1 and σ_2 , while $g = 1.968$ is adopted from the ESR.³⁸ In this way, we arrive at the values that underestimate the experimental result by $\simeq 0.2\mu_B$ (last column of Table V). Since this offset is nearly independent of J'_1/J_1 , the interchain couplings might be the origin of this discrepancy. Indeed, increasing the interchain couplings by a factor of two ($J_{ic2} = -J_{ic1} = 0.04 J_1$) yields $m = 2.49\mu_B$, in excellent agreement with the experiment. However, larger interchain couplings substantially increase the Néel temperature and worsen the agreement between the simulated and experimental $\chi(T)$. Since the experimental value of T_N is more precise than m , we argue that the parameters $J_{ic2} = -J_{ic1} = 0.02 J_1$ are preferable, while the $0.2\mu_B$ deviation between the experimental and simulated values of m is still reasonable. Indeed, the experimental estimate of m relies upon the available magnetic form-factors as well as on the accuracy of the subtraction procedure. Therefore, we can not exclude a systematic experimental error in m that should be verified by neutron experiments on single crystals.

As follows from Table V, different values of J'_1/J_1 yield rather similar T_N and m . This surprisingly robust behavior originates from peculiar properties of spin-3/2 alternating Heisenberg chains that show low spin gaps in the $0.41 < J'_1/J_1 < 1$ range between the critical points at $J'_1/J_1 = 0.41$ and $J'_1/J_1 = 1$, where the spin gap vanishes (see Sec. VI and Ref. 39). To evaluate the optimal J'_1/J_1 , we trace the general trends. First, smaller J'_1/J_1 ratios yield better agreement with the experimental T_N . Second, m is nearly independent of J'_1/J_1 for $J'_1/J_1 \geq 0.5$. Thus, the parametrization $J_1 : J'_1 : J_{ic1} : J_{ic2} \simeq 1 : 0.5 : -0.02 : 0.02$ with $J_1 \simeq 50$ K is the optimal choice, since it conforms to the experimental $\chi(T)$ dependence, accurately reproduces the experimental T_N as well as the g -factor, and is in reasonable agreement with the experimental m .

VI. QUANTUM-CLASSICAL CROSSOVER

For a correct application of classical models, it is crucial to know at which point quantum effects become relevant and the classical approximation breaks down. In this respect, the quasi-1D magnetic model of $\text{Cr}_2[\text{BP}_3\text{O}_{12}]$ is a promising candidate. The leading exchange couplings J_1 and J'_1 form alternating chains, while the interchain couplings are substantially smaller. Besides, $\text{Cr}_2[\text{BP}_3\text{O}_{12}]$ lacks frustration, thus quantum MC simulations can be performed.

First, we study nearest-neighbor spin correlations using QMC and classical MC simulations. The difference between the two results is directly related to quantum

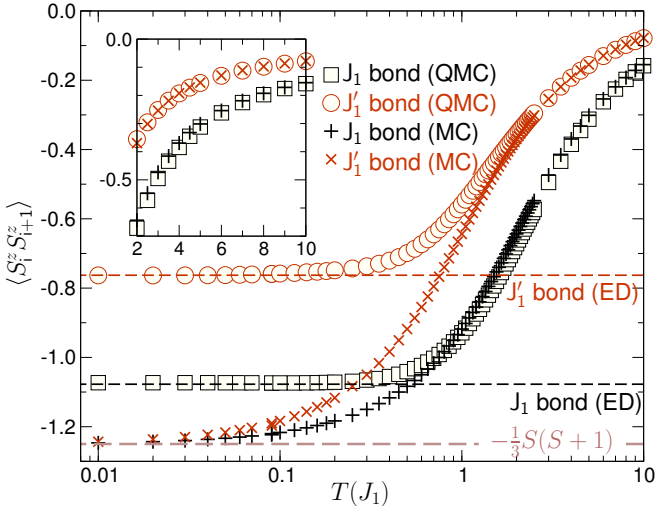


FIG. 6. (Color online) Temperature dependence of the nearest-neighbor diagonal spin correlations $\langle S_i^z S_{i+1}^z \rangle$ in the $S=3/2$ alternating Heisenberg chain model ($J_1'/J_1=0.5$). QMC results are plotted with squares (J_1) and circles (J_1'), the classical MC results are depicted with pluses (J_1) and crosses (J_1'). The dashed lines denote the ED results for the quantum model. The $\frac{1}{3}S(S+1)$ line marks the maximal diagonal correlation for $S=3/2$ spins. Inset: at high temperatures ($T > 2J_1$), the QMC and MC curves become almost indistinguishable.

fluctuations: while QMC correctly accounts for the quantum behavior at finite temperatures, the classical MC method captures thermal fluctuations, only.

In the following, we consider a 1D $J_1 - J_1'$ magnetic model, where the interchain couplings are neglected completely. For $J_1'/J_1=0.5$, we simulate the temperature dependence of the diagonal spin correlations $\langle S_i^z S_{i+1}^z \rangle$ and $\langle S_{i+1}^z S_{i+2}^z \rangle$, where $i=0$ corresponds to the stronger coupling J_1 , while $i=1$ corresponds to J_1' .

The resulting curves are plotted in Fig. 6. In the high-temperature range (see inset in Fig. 6), the classical and quantum results are practically indistinguishable. At $T \simeq J_1$, the curves start to deviate significantly. The classical MC curves exhibit an asymptotic behavior and join at $T=0$. This is in line with a complete elimination of thermal fluctuations, thereby the spin correlations reach their extremal value for $S=3/2$ spins, which amounts to $-[S(S+1)]/3 = -1.25$.

Although the QMC curves exhibit qualitatively similar behavior at low temperatures, they saturate at substantially higher values of $\langle S_i^z S_{i+1}^z \rangle$. Dissimilar to the classical model, the $i=0$ (J_1) and $i=1$ (J_1') QMC curves saturate at different values of $\langle S_i^z S_{i+1}^z \rangle$, indicating the onset of dimerization.

In the vicinity of the broad maximum of the magnetic susceptibility ($T^{\max} \simeq 2J_1$), and even at lower temperatures, the classical MC simulations are in excellent agreement with the quantum model. Therefore, experimental thermodynamic data [e.g., $\chi(T)$ and magnetic specific heat] for $T \geq J_1$ should be well reproduced within the

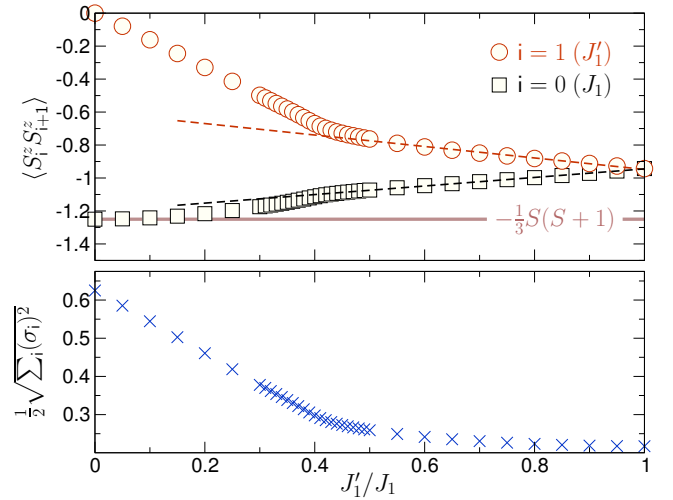


FIG. 7. (Color online) Top: nearest-neighbor diagonal spin correlations $\langle S_i^z S_{i+1}^z \rangle$ in the $S=3/2$ alternating Heisenberg chain model as a function of the alternation ratio J_1'/J_1 at $T=0.03 J_1$. Dashed lines are guides to the eye. Bottom: root mean square of $\sigma_i \equiv (\langle S_i^z S_{i+1}^z \rangle - \frac{1}{3}S(S+1))$ ($i=1, 2$), reflecting the discrepancy between the quantum and the classical models.

classical approximation. This empirical rule follows earlier experimental and numerical results for uniform spin-3/2 chains.⁹ It can also be generalized to quasi-2D and 3D systems, owing to further suppression of quantum fluctuations in higher dimensions. However, in 0D systems, such as isolated dimers, quantum effects are expected to play a more substantial role.

To explore the evolution of quantum fluctuations by a gradual crossover from 1D to 0D regime, we evaluate the GS diagonal spin correlations for different ratios J_1'/J_1 . Although QMC simulations are not applicable at $T=0$, the temperature evolution of spin correlations in Fig. 6 suggests only a marginal change in $\langle S_i^z S_{i+1}^z \rangle$ below $0.03 J_1$. Thus, finite-temperature spin correlations simulated at $T=0.03 J_1$ can be regarded as a rather accurate measure of GS ($T=0$) spin correlations.

Fig. 7 (top) shows the resulting $\langle S_i^z S_{i+1}^z \rangle(J_1'/J_1)$ dependencies. In the uniform-chain limit ($J_1'/J_1=1$), the correlations for $i=0$ and 1 coincide. Dimerization gives rise to a quasilinear behavior observed down to $J_1'/J_1 \simeq 0.4$. At this point, both curves exhibit a pronounced kink, and their further evolution is different: the $i=0$ (J_1) curve rapidly drops almost down to the extremal value $\frac{1}{3}S(S+1)$, while the $i=1$ (J_1') curve exhibits a quasilinear growth up to zero correlation in the $J_1'/J_1=0$ limit. This behavior is remarkably different from the classical case, where the constant spin-spin correlation of $-\frac{1}{3}S(S+1)$ is expected.

To sharpen the crossover at $J_1'/J_1 \simeq 0.4$, we consider root mean square deviation for $\sigma_i \equiv (\langle S_i^z S_{i+1}^z \rangle - \frac{1}{3}S(S+1))$ ($i=1, 2$), which reflects the difference between the quantum and classical models. The resulting dependence is shown in Fig. 7 (bottom). For

$0.5 \leq J'_1/J_1 \leq 1$, only a marginal increase is observed, while at $J'_1/J_1 \simeq 0.4$ the slope changes distinctly. For $J'_1/J_1 < 0.4$, a quasilinear behavior is restored.

The drastic change in the spin-spin correlations around $J'_1/J_1 \simeq 0.4$ indicates the critical point of bond-alternating spin-3/2 chains. While such chains generally have gapped GS, they become gapless in the uniform-chain limit ($J'_1/J_1 = 1$) and at the critical point of $J'_1/J_1 \simeq 0.41$, according to density-matrix renormalization group³⁹ and QMC studies.⁴⁰ Qualitatively, the critical point at $J'_1/J_1 \simeq 0.41$ can be understood as the transition between two different valence-bond-solid (VBS)-type GSs.

The VBS state entails singlet pairs formed by individual spin-1/2 entities comprising spin-3/2 sites of the lattice.⁴¹ Although it is not an exact GS of the Heisenberg Hamiltonian in Eq. (1), the references to relevant VBS states are instrumental in understanding peculiarities of the magnetic behavior. The spin-3/2 chain can form two VBS states, the (3,0) state having three singlet pairs on one bond and no pairs on the contiguous bonds, or the (2,1) state having two singlet pairs on one bond and one singlet pair on each of the neighboring bonds. At low J'_1/J_1 , alternating spin-3/2 chains are close to the (3,0) regime, as shown by the drastic difference between the spin-spin correlations for J_1 and J'_1 . At $J'_1/J_1 > 0.41$, the system resembles the (2,1) VBS⁴⁰ and eventually develops the GS of a uniform spin-3/2 chain with equal correlations on the J_1 and J'_1 bonds (Fig. 7). Note that the low-temperature physics of alternating spin-3/2 chains is essentially governed by quantum effects and can not be reproduced in the classical approximation.

VII. DISCUSSION AND SUMMARY

The formation of alternating spin chains contrasts with the presence of isolated Cr_2O_9 dimers in the crystal structure of $\text{Cr}_2[\text{BP}_3\text{O}_{12}]$. However, such differences between the structure and the ensuing spin lattice are not unusual, especially for phosphates, vanadates, and other compounds with complex anions that are capable of mediating the superexchange. For example, a large superexchange coupling via the PO_4 tetrahedra between the structural dimers is a salient feature of the spin-1/2 alternating-chain magnet $(\text{VO})_2[\text{P}_2\text{O}_7]$ (Ref. 26). In spin-1/2 V^{4+} and Cu^{2+} compounds, interdimer couplings often exceed the intradimer exchange, whereas the latter is small or even negligible, as in $\text{Cu}_2[\text{P}_2\text{O}_7]$ (Ref. 28) or $\text{VO}[\text{HPO}_4] \cdot \frac{1}{2}\text{H}_2\text{O}$ (Ref. 42).

The $\text{Cr}_2[\text{BP}_3\text{O}_{12}]$ case is different, though, because the intradimer coupling J_1 exceeds the interdimer coupling J'_1 . The reason behind the sizable intradimer coupling is the strong direct exchange that was previously observed in LiCrO_2 .³² While the Cr–O–Cr angles amount to 87.8° and impede the AF superexchange, the direct overlap of Cr d orbitals is strong enough to facilitate the sizable AF J_1 . This mechanism is not operative in typical spin-

1/2 systems with structural dimers, because V^{4+} cations form VO_5 square pyramids and remain on opposite sides of the basal plane of such pyramids, thus featuring only a weak direct overlap of the magnetic d_{xy} orbitals. In the case of Cu^{2+} , the magnetic orbital has the $d_{x^2-y^2}$ symmetry, unfavorable for the direct overlap.

It is also instructive to compare different interdimer couplings in $\text{Cr}_2[\text{BP}_3\text{O}_{12}]$. Similar to other transition-metal phosphates,^{27,28} the Cr-based Wannier functions show sizable contributions of Cr 3d and O 2p states, only (Fig. 5). Phosphorous states weakly contribute to the magnetic orbitals and play a minor role in the superexchange running via the Cr–O...O–Cr pathways. The efficiency of these pathways intimately depends on details of the crystal structure.

Remarkably, $\text{Cr}_2[\text{BP}_3\text{O}_{12}]$ not only entails the spin lattice of alternating chains, but also features the alternation ratio of $J'_1/J_1 \simeq 0.5$, which is close to the critical point with the gapless ground state at $J'_1/J_1 \simeq 0.41$. The proximity to this critical point is one of the reasons behind the long-range AF ordering and the sizable Néel temperature in $\text{Cr}_2[\text{BP}_3\text{O}_{12}]$. Spin-1/2 systems with the larger $J'_1/J_1 \simeq 0.6$ (i.e., weaker dimerization) and comparable interchain couplings⁴³ still have the spin-gap ground state, as in $\text{Pb}_2[\text{V}_3\text{O}_9]$ (Ref. 44) and $\text{Ag}(\text{VO})[\text{AsO}_4]$ (Ref. 45). The large number of interchain couplings per magnetic site (the coordination number amounts to six and three for J_{ic1} and J_{ic2} , respectively), as found in $\text{Cr}_2[\text{BP}_3\text{O}_{12}]$, may also reduce quantum fluctuations. By contrast, an isolated alternating $S = 3/2$ chain with $J'_1/J_1 \simeq 0.5$ would feature an excitation gap of $\sim 0.25 J_1$ with no long-range order.⁴⁰

While the critical point at $J'_1/J_1 \simeq 0.41$ has been widely studied theoretically,^{39,40} experimental probes of this regime and even experimental examples of spin-3/2 alternating chains have not been reported. Therefore, $\text{Cr}_2[\text{BP}_3\text{O}_{12}]$ may be interesting as an experimentally available spin-3/2 alternating-chain system in the vicinity of this critical point. Although $\text{Cr}_2[\text{BP}_3\text{O}_{12}]$ is not perfectly 1D and features the long-range AF order owing to non-zero interchain couplings, an experimental study of spin-spin correlations with, e.g., inelastic neutron scattering, could be instructive. Moreover, the application of external pressure might change the J'_1/J_1 ratio, thus giving access to the peculiar evolution of spin-spin correlations across the critical point (Fig. 7). Detailed studies of the isostructural phase $\text{Fe}_2[\text{BP}_3\text{O}_{12}]$ (Ref. 23) may be instructive as well, because this compound should feature a similar spin lattice in the more classical regime of spin-5/2.

In summary, we extensively characterized the magnetic behavior of $\text{Cr}_2[\text{BP}_3\text{O}_{12}]$ using magnetic susceptibility, neutron diffraction, and ESR measurements. The long-range AF order established below $T_N = 28 \text{ K}$ is described with the propagation vector $\mathbf{k} = 0$, whereby the spins on nearest-neighbor Cr atoms within the ab plane as well as along the c -axis direction are antiparallel. On the microscopic level, $\text{Cr}_2[\text{BP}_3\text{O}_{12}]$ features $S = 3/2$ Heisen-

berg chains with an alternation of the nearest neighbor couplings J_1 and J'_1 . The ratio $J'_1/J_1 \simeq 0.5$ renders $\text{Cr}_2[\text{BP}_3\text{O}_{12}]$ as an interesting model system lying close to the critical point at $J'_1/J_1 \simeq 0.41$, where the spin-3/2 alternating chain has the gapless ground state. The chains are coupled by two nonequivalent interchain exchanges: the FM J_{ic1} and the AF J_{ic2} , both of the order of 1–2 K. The microscopic model is in excellent agreement with the experimental magnetic structure (see Fig. 1): the nearest-neighbor spins within a chain are antiparallel, in accord with the AF nature of J_1 and J'_1 . Moreover, even the interchain coupling regime is compatible with FM J_{ic1} and AF J_{ic2} , thus $\text{Cr}_2[\text{BP}_3\text{O}_{12}]$ lacks any

appreciable frustration effects.

ACKNOWLEDGEMENTS

We are grateful to Yurii Prots and Horst Borrmann for X-ray diffraction measurements, and Alim Ormezi for fruitful discussions. SC, ZJZ, MBT and JTZ acknowledge the financial support from CAS/SAFEA International Partnership program for Creative Research Teams (grant number 51121064) and the MPG-CAS partner group. A. A. T. was supported by the Alexander von Humboldt Foundation and the Mobilitas grant MTT-77 of the ESF.

-
- * janson@cpfs.mpg.de
 † altsirlin@gmail.com
 ‡ rosner@cpfs.mpg.de
- ¹ H. Bethe, *Z. Phys. A* **71**, 205 (1931); C. K. Majumdar and D. K. Ghosh, *J. Math. Phys.* **10**, 1388 (1969); *J. Math. Phys.* **10**, 1399 (1969).
 - ² B. S. Shastry and B. Sutherland, *Physica B+C* **108**, 1069 (1981).
 - ³ R. Dingle, M. E. Lines, and S. L. Holt, *Phys. Rev.* **187**, 643 (1969); M. T. Hutchings, G. Shirane, R. J. Birgeneau, and S. L. Holt, *Phys. Rev. B* **5**, 1999 (1972).
 - ⁴ W. J. M. de Jonge, J. P. A. M. Hijmans, F. Boersma, J. C. Schouten, and K. Kopinga, *Phys. Rev. B* **17**, 2922 (1978).
 - ⁵ S. Itoh, H. Tanaka, and T. Otomo, *J. Phys. Soc. Jpn.* **66**, 455 (1997); S. Itoh, H. Tanaka, and M. J. Bull, *J. Phys. Soc. Jpn.* **71**, 1148 (2002).
 - ⁶ For example: P. Chandra and B. Doucot, *Phys. Rev. B* **38**, 9335 (1988); E. Dagotto and A. Moreo, *Phys. Rev. B* **39**, 4744 (1989).
 - ⁷ For example: I. Rousochatzakis, A. M. Läuchli, and R. Moessner, *Phys. Rev. B* **85**, 104415 (2012).
 - ⁸ F. Haldane, *Phys. Rev. Lett.* **50**, 1153 (1983).
 - ⁹ S. Itoh, Y. Endoh, K. Kakurai, and H. Tanaka, *Phys. Rev. Lett.* **74**, 2375 (1995); S. Itoh, Y. Endoh, K. Kakurai, H. Tanaka, S. M. Bennington, T. G. Perring, K. Ohoyama, M. J. Harris, K. Nakajima, and C. D. Frost, *Phys. Rev. B* **59**, 14406 (1999).
 - ¹⁰ C. Payen, H. Mutka, J. Soubeyroux, P. Molinié, and P. Colombet, *J. Magn. Magn. Mater.* **104-107**, 797 (1992); H. Mutka, C. Payen, and P. Molinie, *Europhys. Lett.* **21**, 623 (1993).
 - ¹¹ M. P. Pechini, (1967), U.S. patent 3.330.397.
 - ¹² J.-X. Mi, J.-T. Zhao, S.-Y. Mao, Y.-X. Huang, H. Engelhardt, and R. Kniep, *Z. Kristallogr. New Cryst. Struct.* **215**, 201 (2000).
 - ¹³ The ^{11}B -containing chemical ($\text{H}_3^{11}\text{BO}_3$) has been used to prepare a sample for neutron powder diffraction.
 - ¹⁴ A. Larson and R. von Dreele, “General structure analysis system (GSAS),” Los Alamos National Laboratory Report LAUR 86-748 (1994).
 - ¹⁵ J. Rodríguez-Carvajal, *Physica B* **192**, 55 (1993).
 - ¹⁶ K. Koepernik and H. Eschrig, *Phys. Rev. B* **59**, 1743 (1999).
 - ¹⁷ G. Kresse and J. Furthmüller, *Phys. Rev. B* **54**, 11169 (1996); *Comput. Mater. Sci.* **6**, 15 (1996).
 - ¹⁸ J. P. Perdew and Y. Wang, *Phys. Rev. B* **45**, 13244 (1992).
 - ¹⁹ J. P. Perdew, K. Burke, and M. Ernzerhof, *Phys. Rev. Lett.* **77**, 3865 (1996).
 - ²⁰ J. Heyd, G. E. Scuseria, and M. Ernzerhof, *J. Chem. Phys.* **118**, 8207 (2003); J. Heyd and G. E. Scuseria, *J. Chem. Phys.* **121**, 1187 (2004).
 - ²¹ Large computational demands incurred by the hybrid functionals lead to severe restrictions on the number of k points. Nevertheless, the results obtained on a sparse k mesh are sufficiently accurate and well-converged, owing to the insulating nature of $\text{Cr}_2[\text{BP}_3\text{O}_{12}]$.
 - ²² A. Albuquerque, F. Alet, P. Corboz, P. Dayal, A. Feiguin, S. Fuchs, L. Gamper, E. Gull, S. Gürtler, A. Honecker, R. Igarashi, M. Körner, A. Kozhevnikov, A. Läuchli, S. R. Manmana, M. Matsumoto, I. P. McCulloch, F. Michel, R. M. Noack, G. Pawłowski, L. Pollet, T. Pruschke, U. Schollwöck, S. Todo, S. Trebst, M. Troyer, P. Werner, and S. Wessel, *J. Magn. Magn. Mater.* **310**, 1187 (2007), arXiv:0801.1765.
 - ²³ W.-L. Zhang, C.-S. Lin, L. Geng, Y.-Y. Li, H. Zhang, Z.-Z. He, and W.-D. Cheng, *J. Solid State Chem.* **183**, 1108 (2010); F. F. Li, H. J. Zhang, and L. N. Zhang, *Acta Cryst.* **E66**, i63 (2010).
 - ²⁴ M. Campostrini, M. Hasenbusch, A. Pelissetto, P. Rossi, and E. Vicari, *Phys. Rev. B* **65**, 144520 (2002), cond-mat/0110336; A. Pelissetto and E. Vicari, *Phys. Rep.* **368**, 549 (2002), cond-mat/0012164.
 - ²⁵ See Supplementary information for the refined neutron diffraction patterns, for the crystal structure refinement, ESR data, low-temperature magnetization data, as well as LSDA and GGA density of states for the ferromagnetic solution.
 - ²⁶ A. W. Garrett, S. E. Nagler, D. A. Tennant, B. C. Sales, and T. Barnes, *Phys. Rev. Lett.* **79**, 745 (1997).
 - ²⁷ A. A. Tsirlin, R. Nath, C. Geibel, and H. Rosner, *Phys. Rev. B* **77**, 104436 (2008), arXiv:0802.2293.
 - ²⁸ O. Janson, A. A. Tsirlin, J. Sichelschmidt, Y. Skourski, F. Weickert, and H. Rosner, *Phys. Rev. B* **83**, 094435 (2011), arXiv:1011.5393; S. Lebernegg, A. A. Tsirlin, O. Janson, R. Nath, J. Sichelschmidt, Y. Skourski, G. Amthauer, and H. Rosner, *Phys. Rev. B* **84**, 174436 (2011), arXiv:1107.0250.

- ²⁹ Here, we do not adapt the local coordinate frame to the global symmetry of the crystal structure, and direct the local z axis along one of the Cr–O bonds (see also Fig. 5). Therefore, the resulting d states do not show the weak splitting in the t_{2g} subspace, as expected for trigonally distorted octahedron. This simplification does not affect any of our results, because Cr^{3+} shows the robust high-spin state with the half-filled t_{2g} levels, whereas fine structure of these levels has minor effect on the magnetism.
- ³⁰ D. C. Johnston, R. K. Kremer, M. Troyer, X. Wang, A. Klümper, S. L. Bud'ko, A. F. Panchula, and P. C. Canfield, *Phys. Rev. B* **61**, 9558 (2000), [cond-mat/0003271](#).
- ³¹ M. T. Czyżyk and G. A. Sawatzky, *Phys. Rev. B* **49**, 14211 (1994).
- ³² I. I. Mazin, *Phys. Rev. B* **75**, 094407 (2007), [arXiv:cond-mat/0701520](#).
- ³³ C. J. Fennie and K. M. Rabe, *Phys. Rev. Lett.* **96**, 205505 (2006), [cond-mat/0602503](#).
- ³⁴ C. Franchini, R. Podloucky, J. Paier, M. Marsman, and G. Kresse, *Phys. Rev. B* **75**, 195128 (2007); F. Iori, M. Gatti, and A. Rubio, *Phys. Rev. B* **85**, 115129 (2012), [arXiv:1201.3308](#).
- ³⁵ It is widely believed that for insulators only the FLL DC correction is appropriate. By the same token, thorough studies of magnetic couplings in Cu and V oxides show that AMF may provide comparable or even better results than FLL, although in a rather unsystematic fashion: see, e.g., A. A. Tsirlin, O. Janson, and H. Rosner, *Phys. Rev. B* **82**, 144416 (2010), [arXiv:1007.1646](#); *Phys. Rev. B* **84**, 144429 (2011), [arXiv:1104.2495](#).
- ³⁶ For the fitting, we used the experimental data above $T_N = 28$ K, since a one-dimensional model cannot account for the AF ordering (Ref. 37).
- ³⁷ N. D. Mermin and H. Wagner, *Phys. Rev. Lett.* **17**, 1133 (1966).
- ³⁸ Unfortunately, the quasi-1D character of the magnetic model requires $L_z \gg L_x \simeq L_y$ for an N -site lattice ($N = L_x \times L_y \times L_z$). This leads to a small number of computationally feasible lattices, impeding an accurate estimation of the magnetic moment. To check the results for consistency, we repeated the fitting using a simplified scaling $\sigma_2 = 0$. As expected, the σ_1 values are substantially renormalized. Yet, both approaches yield marginally different values of S_∞ ($\sim 1\%$ difference).
- ³⁹ M. Yajima and M. Takahashi, *J. Phys. Soc. Jpn.* **65**, 39 (1996).
- ⁴⁰ S. Yamamoto, *Phys. Rev. B* **55**, 3603 (1997).
- ⁴¹ I. Affleck, T. Kennedy, E. H. Lieb, and H. Tasaki, *Phys. Rev. Lett.* **59**, 799 (1987); *Comm. Math. Phys.* **115**, 477 (1988).
- ⁴² D. A. Tennant, S. E. Nagler, A. W. Garrett, T. Barnes, and C. C. Torardi, *Phys. Rev. Lett.* **78**, 4998 (1997), [cond-mat/9704093](#).
- ⁴³ The interchain couplings should be considered irrespective of their sign and together with the relevant coordination numbers. In $\text{Cr}_2[\text{BP}_3\text{O}_{12}]$, the effective interchain coupling is $J_{\text{eff}} = 3J_{\text{ic}2} + 6|J_{\text{ic}1}| = 0.18J_1$, i.e., $J_{\text{ic}}/J_1 = 0.09$ for the typical coordination number of 2 as, e.g., in $\text{Pb}_2[\text{V}_3\text{O}_9]$.
- ⁴⁴ A. A. Tsirlin and H. Rosner, *Phys. Rev. B* **83**, 064415 (2011), [arXiv:1011.3981](#).
- ⁴⁵ A. A. Tsirlin, R. Nath, J. Sichelschmidt, Y. Skourski, C. Geibel, and H. Rosner, *Phys. Rev. B* **83**, 144412 (2011), [arXiv:1101.2546](#).
-

Supplementary information for
Structure and magnetism of $\text{Cr}_2[\text{BP}_3\text{O}_{12}]$:
 Towards the “quantum–classical” crossover in a spin-3/2 alternating chain

O. Janson, S. Chen, A. A. Tsirlin, S. Hoffmann, J. Sichelschmidt,
 Q. Huang, Z.-J. Zhang, M.-B. Tang, J.-T. Zhao, R. Kniep, H. Rosner

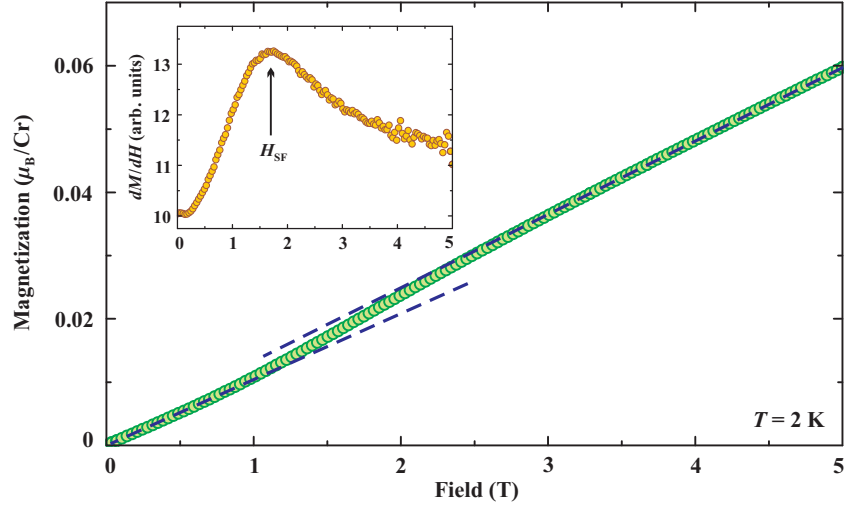


FIG. S1. Field dependence of the magnetization of $\text{Cr}_2[\text{BP}_3\text{O}_{12}]$ measured at 2 K. The lines are guide-for-the-eye. The inset shows the field derivative of the magnetization.

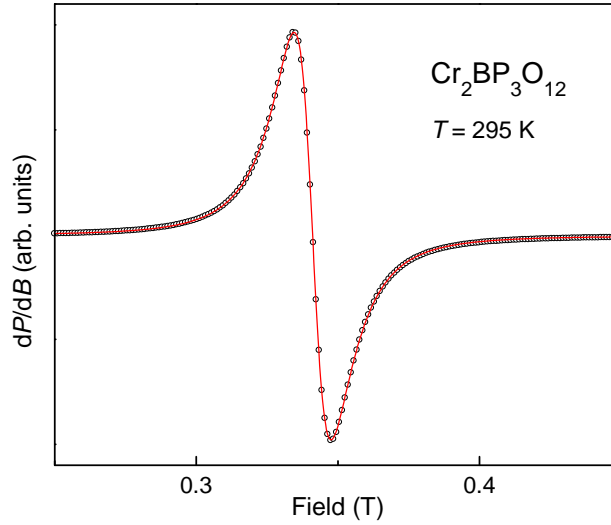


FIG. S2. Electron spin resonance spectrum (circles; first derivative of absorbed microwave power dP/dB) taken at 9.5 GHz (X-band). Solid line denotes a powder-averaged Lorentzian line with $g_{\perp} \approx g_{\parallel} = 1.9680 \pm 0.0005$ and linewidth $\Delta B_{\perp} = 8.6 \pm 0.2$ mT and $\Delta B_{\parallel} = 18.8 \pm 0.2$ mT.

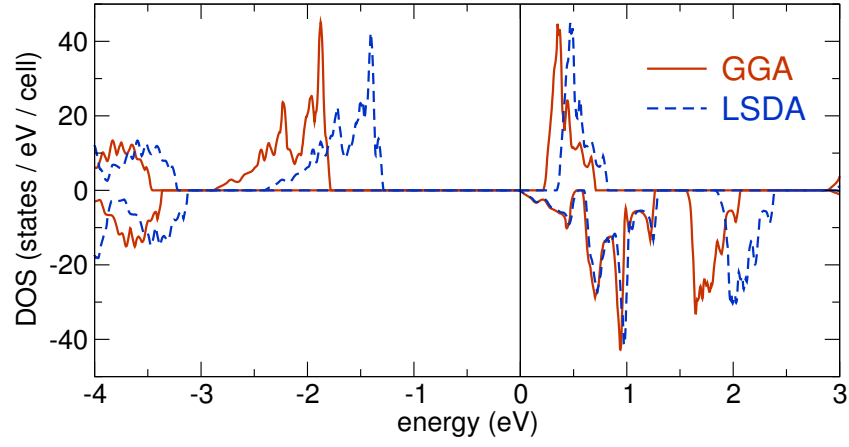


FIG. S3. Cr₂[BP₃O₁₂]: GGA (solid line) and LSDA (dashed line) density of states for the ferromagnetic solution. Positive and negative values refer to the majority and minority spin channel, respectively. Note the different values of the band gap: -1.78 eV in GGA and -1.29 eV in LSDA.

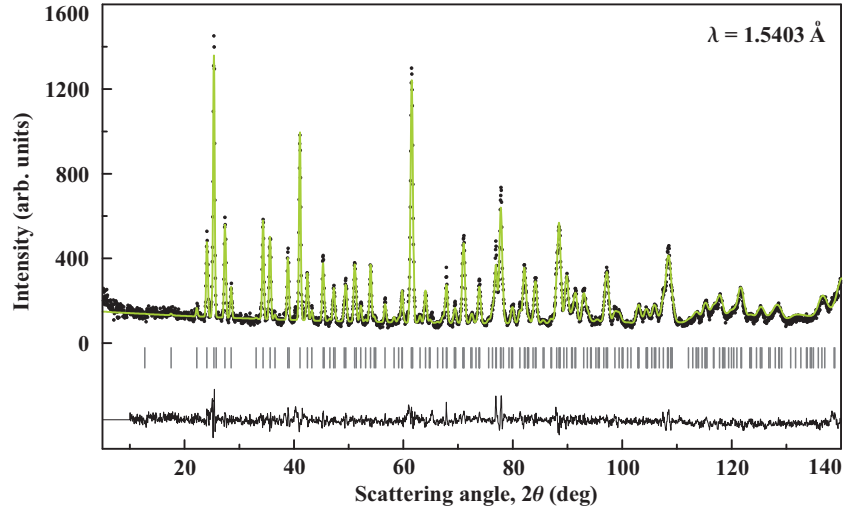


FIG. S4. Rietveld refinement of the neutron diffraction data collected at 35 K. Ticks show the reflection positions.